Preclinical evaluation of [^{11}C]CHDI-009R for quantification of mutant huntingtin aggregates

Authors

Franziska Zajicek[1,2], Liesbeth Everix[1,2], Annemie Van Eetveldt[1,2], Jeroen Verhaeghe[1,2], Stef De Lombaerde[1,3], Alan Miranda[1,2], Jordy Akkermans[1,2], Celia Dominguez[4], Vinod Khetarpal[4], Jonathan Bard[4], Longbin Liu[4], Steven Staelens[1,2], Daniele Bertoglio[2,5]

[1]Molecular Imaging Center Antwerp (MICA), University of Antwerp, Antwerp, Belgium

[2]μNeuro Research Center of Excellence, University of Antwerp, Antwerp, Belgium

[3]Department of Nuclear Medicine, Antwerp University Hospital, Antwerp, Belgium

[4]CHDI Management, Inc., the company that manages the scientific activities of CHDI Foundation, Inc., Los Angeles, CA, USA

[5]Bio-Imaging Lab, University of Antwerp, Antwerp, Belgium

Corresponding author:

Dr. Daniele Bertoglio

Bio-Imaging Lab, Faculty of Pharmaceutical, Biomedical and Veterinary Sciences,

University of Antwerp, Universiteitsplein 1, Wilrijk, Belgium

Tel. +32 3 265 8736

Email: daniele.bertoglio@uantwerpen.be

ORCID

Franziska Zajicek: 0000-0001-5410-687X

Liesbeth Everix: 0000-0001-5985-1609

Annemie Van Eetveldt: 0000-0002-6488-5456

Jeroen Verhaeghe: 0000-0002-4493-1902

Stef De Lombaerde: 0000-0002-5307-3575

Alan Miranda: 0000-0002-5381-015X

Jordy Akkermans: 0000-0002-1533-9504

Vinod Khetarpal: 0000-0002-2175-5117

Jonathan Bard: 0000-0002-5097-1361

Longbin Liu: 0000-0003-3995-0196

Steven Staelens: 0000-0003-3376-0519

Daniele Bertoglio: 0000-0003-4205-5432

Keywords

Positron Emission Tomography; Huntington's disease; kinetic modeling; mHTT aggregates; [^{11}C]CHDI-009R; zQ175DN

Abstract

Huntington's disease (HD) is a neurodegenerative disorder caused by an expanded trinucleotide repeat in the huntingtin gene (*HTT*) that subsequently leads to aggregation of the mutant huntingtin (mHTT) protein. Thus, lowering mHTT is a key therapeutic approach used by several candidate therapeutics currently under investigation. Visualization of the efficiency of these therapeutics through *in vivo* mHTT quantification rises in importance. For positron emission tomography (PET) imaging of mHTT aggregates, it is critical to characterize the *in vivo* kinetic profile of newly identified mHTT binders to assess their translational application. Here, we report the evaluation of [^{11}C]CHDI-009R, a PET imaging radioligand with higher affinity and selectivity for mHTT aggregates than previously reported radioligands, in the heterozygous (HET) zQ175DN mouse model of HD and wild-type (WT) littermates at 9 and 3 months of age.

[^{11}C]CHDI-009R displayed high stability in plasma and brain, which was reflected in brain kinetics as demonstrated by rapid uptake followed by relatively slow elimination. Kinetic modeling and volume of distribution $V_{T\ (IDIF)}$ indicated the radioligand's ability to quantify mHTT aggregation at 9 months of age with clear genotype differentiation ($p<0.0001$). [^{11}C]CHDI-009R showed an excellent test-retest reliability in 9-month-old mice (intraclass correlation coefficient: 0.62 - 0.79). A phenotypic difference in mHTT aggregates was also observed in 3-month-old mice in several brain structures ($p<0.05$) and was confirmed with [^{3}H]CHDI-009R autoradiography.

Overall, this study suggests [^{11}C]CHDI-009R is a promising radioligand for the detection of cerebral mHTT aggregates in a mouse model of HD and supports its advance to clinical evaluation.

Introduction

Huntington's disease (HD) is a progressive neurodegenerative disorder caused by an expanded trinucleotide (CAG) repeat in exon 1 of the huntingtin (*HTT*) gene. The transcription and translation of mutant *HTT* leads to the aggregation of mutant huntingtin (mHTT) protein [1, 2], which, alongside mHTT fragments, is involved in cellular dysfunction and loss of neurons [3, 4]. With several disease-modifying therapeutic interventions aimed to lower mHTT expression under clinical investigation [5-7] (e.g. ClinicalTrials.gov identifier (ID): NCT06024265; NCT05032196), there is an increasing interest in accurately quantifying their ameliorative effect. Currently, the estimate of the central nervous system (CNS) target engagement of HTT-lowering therapeutics is indirect, relying on extrapolations of soluble HTT levels in non-brain compartments, such as cerebrospinal fluid, both in the preclinical [8] and clinical setting [9] (www.clinicaltrials.gov, identifier NCT02519036). Still, fluid biomarkers lack brain region-specific information that positron emission tomography (PET) imaging of mHTT aggregates could provide. Thus, PET imaging holds great potential as a complementary tool to assess brain region-specific target engagement, as previously demonstrated preclinically [10]. Thus, enabling accurate spatial and temporal evaluation of efficacy with potential therapeutic interventions.

We recently described a number of novel radiotracers for mHTT aggregate imaging in preclinical imaging studies, namely [^{11}C]CHDI-626 [11-13], [^{11}C]CHDI-180R [10, 12, 14, 15] and [^{18}F]CHDI-650 [16, 17] with varying levels of applicability in mice. Additionally, [^{11}C]CHDI-626 [18] was advanced to the clinic but later discontinued due to an undesirable brain uptake and decay profile. On the other hand, [^{11}C]CHDI-180R detected a significant difference between people with HD (PwHD) and healthy controls; however, it also displayed high intersubject variability [19]. Thus, a more suited clinical candidate would be preferred, and the identification of novel radioligands targeting mHTT aggregates with superior PET radiotracer properties remains a priority. Especially regarding clinical importance, enhanced sensitivity of

91 mHTT aggregate detection in 3-month-old zQ175DN heterozygous (HET) mice is desired, as
92 mHTT aggregation is expected to be lower in abundance in humans than in mouse models.
93 Therefore, we report on the investigation of a novel radioligand, [^{11}C]CHDI-009R, that has
94 been shown to have an almost 3-fold higher maximum binding capacity than CHDI-180R
95 based on autoradiography studies in homozygous zQ175DN brains [20]. Here, we
96 characterize the *in vivo* performance of this tracer in wildtype (WT) and HET zQ175DN knock-
97 in mice through radiometabolite analysis, test-retest variability estimation, quantitative
98 phenotypic comparison at two different ages, and post-mortem autoradiography.
99

100 # Methods

101 ## Animals

102 A total of 63 nine-month-old male HET (*n*=33) and WT (*n*=30) as well as 44 three-month-old
103 male HET (*n*=24) and WT (*n*=20) zQ175DN mice (B6.129S1-*Htt*$^{tm1.1Mfc}$/190ChdiJ JAX stock
104 #029928), were obtained from Jackson Laboratories (Bar Harbour, Maine, USA) [21, 22]. Due
105 to sporadic congenital portosystemic shunt occurring in C57BL/6J mice [23], all animals were
106 screened at Jackson Laboratories before shipment, and hence, all animals used in this study
107 were shunt-free. Study design, group size, body weight, and age of the animals are reported
108 in Fig. 1 and Tables S1-S3. Animals were single-housed at 9 months of age and group-housed
109 at 3 months of age in ventilated cages under a 12 h light/dark cycle. While group-housing is
110 generally considered to achieve better social well-being for mice, minimising aggression and
111 potential injuries caused by dominant-submissive behaviour was prioritised for animals
112 undergoing several imaging sessions. The animals were kept in a temperature- and humidity-
113 controlled environment with food and water *ad libitum*. The animals were given at least one
114 week for acclimatization after arrival before the start of any procedure. Experiments followed
115 the European Committee (decree 2010/63/CEE) and were approved by the Ethical Committee
116 for Animal Testing (ECD 2019-39) at the University of Antwerp (Belgium).

117

118 ## Radioligand synthesis

119 [^{11}C]CHDI-009R was prepared using an automated synthesis module (Carbonsynthon I,
120 Comecer, The Netherlands). The radioligand was prepared via single-step carbon-11 labeling
121 at the pyridazinone-NH site, starting with a solution of the precursor (0.3 mg) in DMF (0.5 ml),
122 which was reacted with excess of [^{11}C]CH_3OTf in the presence of NaOH (1 M, 5 μl) for 3 min
123 at room temperature. To terminate the reaction and to ensure good retention of the compound
124 of interest on the semi-preparative HPLC column, acetonitrile/water (35:65, v/v, 2 ml) was
125 introduced to the reaction mixture, and the resulting crude product was purified on HPLC using

126 an ACE 5 C18-HL 250x10 mm column (ACE, UK), eluted with a mixture of ammonium formate
127 (0.1 M) in acetonitrile (35/65, v/v) as mobile phase, at a flow rate of 6 ml/min. The collected
128 fraction was diluted with water (20 ml) before being loaded on a 1 cc 10 mg Oasis HLB
129 cartridge (Waters, MA, USA). The cartridge was washed with water for injection (3 ml) and
130 eluted through a sterile filter with ethanol (0.5 ml) and saline (4.5 ml) to afford the final product
131 solution.
132 The radiochemical purity of the produced [^{11}C]CHDI-009R was determined using a Kinetex
133 EVO C18, 5μm, 150×4.6 mm (Phenomenex, USA) HPLC column, with a solution of sodium
134 acetate (NaOAc) (0.05 M, pH 5.5) in acetonitrile/ (30:70, v/v) as mobile phase, at a flow of 1
135 ml/min, with UV absorbance set at 289 nm. Based on 37 productions, radiochemical purity
136 was greater than 99%, a molar activity (A_m) of 93.59±27.61 GBq/μmol, and a radiochemical
137 yield of 7.83±0.03% was achieved.
138
139 **Radiometabolite analysis**
140 Evaluation of *in vivo* plasma and brain radiometabolite profiles was performed at 5, 20, and
141 40 min post-injection (p.i.). Mice were injected via the lateral tail vein with [^{11}C]CHDI-009R
142 (WT: 3.78±0.87 MBq; HET: 3.75±0.62 MBq in 200 µl), and blood was withdrawn via cardiac
143 puncture at designated times, and brains were immediately excised. The homogenization and
144 extraction were conducted as previously described [10, 17]. The extraction efficiency from
145 plasma samples (percentage of recovery of radioactivity) was 98.4±2.6%, whereas in brain
146 samples, an extraction efficiency of 100.6±4.7% was achieved. Plasma or brain supernatant
147 was loaded onto a pre-conditioned reverse-phase (RP)-HPLC system (Luna C18(2), 5 µm
148 HPLC column (250x4.6 mm) + Phenomenex security guard pre-column) and eluted with
149 NaOAc 0.05M pH 5.5 and acetonitrile: (87:13 for 10 min v/v) buffer at a flow rate of 1 ml/min.
150 RP-HPLC fractions were collected at 0.5 min intervals for 10 min. Pure tracer (5μCi) was
151 loaded onto the same HPLC setup (Fig. S1). Control experiments confirmed that no apparent

152 degradation of the radiotracer occurred during procedural work-up in both plasma
153 (99.91±0.00% of intact tracer) and brain (92.14±0.07% of intact tracer).
154

155 **Dynamic PET imaging acquisition**

156 Dynamic microPET/Computed tomography (CT) images were acquired on Siemens Inveon
157 PET-CT scanners (Siemens Preclinical Solution, Knoxville, USA). Animal preparation was
158 performed as previously described [10, 24]. Animal and dosing information for both WT and
159 HET mice of all paradigms are given in the supplementary Tables S1-S3.
160 PET data were acquired in list mode format. Following the microPET scan, a 10 min 80 kV/500
161 µA CT scan was performed for attenuation and scatter correction. The same microPET scan,
162 was also used to estimate the blood radioactivity through a non-invasive image-derived input
163 function (IDIF) to estimate the volume of distribution ($V_{T\ (IDIF)}$) as a surrogate of V_T.
164 Acquired PET data were reconstructed into 39 frames of increasing length (12x10s, 3x20s,
165 3x30s, 3x60s, 3x150s, and 15x300s). Images were reconstructed using a list-mode iterative
166 reconstruction proprietary spatially variant resolution modeling in 8 iterations and 16 subsets
167 of the 3D ordered subset expectation maximization (OSEM 3D) algorithm [25]. Normalization,
168 dead time, and CT-based attenuation corrections were applied, and PET image frames were
169 reconstructed on a 128x128x159 grid with 0.776x0.776x0.796 mm^3 voxels.
170

171 **Image processing and analysis**

172 Image processing and analysis were performed with PMOD 3.6 software (PMOD
173 Technologies, Zurich, Switzerland) as previously described [11]. For spatial normalization of
174 the PET/CT images, brain normalization of the CT image to a CT template was performed by
175 adapting the previously described protocol [26]. We applied the volumes-of-interest (VOIs)
176 described in previous studies [10, 11], adapted from the Waxholm atlas [27]. Using those VOIs,
177 time activity curves (TACs) were then extracted for individual brain regions. The IDIFs were

178 extracted from the PET images by generating a VOI in the lumen of the left ventricle at an
179 early time frame exhibiting maximal activity in the heart and applying a threshold of 50% of the
180 max signal as previously described [24, 28-30]. Standardized uptake value (SUV) was
181 calculated as activity concentration [kBq/cc] divided by injected dose [kBq] per body weight
182 [g].
183 These regional TACs and IDIFs were used to estimate $V_{T\ (IDIF)}$ values through kinetic modeling.
184 $V_{T\ (IDIF)}$ was estimated by fitting the extracted TACs with standard two-tissue compartmental
185 model (2TCM), with blood volume fraction (V_B) fixed at 3.6% [10, 11] and Logan linear model
186 to calculate $V_{T\ (IDIF)}$. Pixelwise kinetic modeling was performed using the Logan graphical
187 analysis in PXMOD (PMOD 4.2). The averaged parametric maps were subsequently overlaid
188 onto a Waxholm MRI template.
189

190 **Tissue collection for Autoradiography**

191 Animals were euthanized by decapitation while under anaesthesia. Brains were dissected and
192 fresh-frozen in 2-metylbuthane at −35°C for 2 min and preserved at −80°C. Coronal sections
193 of 10 μm thickness were collected at 1.10 mm from the bregma according to Paxinos and
194 Franklin [31] in triplicate using a cryostat (Leica, Germany) on Superfrost Plus slides (Thermo
195 Fischer Scientific, USA).
196

197 **Autoradiography**

198 [^{3}H]CHDI-009R was provided by Novandi Chemistry AB (Sweden) with a A_m of 82 Ci/mmol.
199 Sections were air-dried at room temperature, pre-incubated for 20 min with binding buffer
200 (50mM Tris-HCl + 120mM NaCl + 5mM KCl + 2mM $CaCl_2$ + 1mM $MgCl_2$, pH 7,4) and air-dried
201 using warm airflow. Dried sections were subsequently incubated with total binding (TB)
202 solution (0.5 nM of [^{3}H]CHDI-009R in binding buffer) and non-specific binding (NSB) solution
203 (0.5 nM of [^{3}H]CHDI-009R + 10 μM of cold ligand in binding buffer) for 1h at room temperature.

204 Subsequently, sections were washed three times for 10 min in ice-cold washing buffer (50mM
205 Tris-HCl, pH 7,4), followed by a brief wash in ice-cold distilled water, and dried for 2h at room
206 temperature. Finally, all sections were exposed on imaging plates (BAS-TR2025, Fujifilm,
207 Japan) for 120 min. Radioactivity was detected with a phosphor imager (Fuji FLA-7000 image
208 reader) and quantified based on intensity values calculated using commercial tritium
209 standards (American Radiolabelled Chemicals Inc., USA). For all samples, the entire surface
210 of the coronal brain slice was used for quantification. The specific binding (SB) was determined
211 by subtracting NSB from TB, which were both measured in triplicate and subsequently
212 averaged. The SB averages were used for statistical analysis. SB was set to 0 if the values of
213 NSB and TB were below the limit of detectability of the calibration curve. Analysis was
214 performed blind to conditions in Fiji, ImageJ (National Institute of Health, USA, version: 2.1).
215

216 **Statistical analysis**

217 The Shapiro-Wilk test revealed that *in vivo* data were normally distributed, while *in vitro* data
218 demonstrated a non-Gaussian distribution; therefore, non-parametric testing was performed
219 on *in vitro* data. All data was visually inspected for outliers, followed, if necessary, by statistical
220 outlier testing with ROUT (Q=0.5%). Two outliers in motor cortex for 9-month-old HET mice
221 were identified and excluded. A Pearson's correlation with simple linear regression was
222 applied to $V_{T\ (IDIF)}$ values from 2TCM and Logan kinetic modeling for model verification. A
223 Spearman's correlation with interpolation (sigmoidal, 4PL, X is concentration) was applied to
224 injected masses and $V_{T\ (IDIF)}$ values from Logan for visualization of a potential mass dose
225 effect. Regular two-way ANOVA with *post hoc* Bonferroni correction for multiple comparisons
226 was applied to analyze $V_{T\ (IDIF)}$ value differences between genotypes.
227 The individual relative test-retest variability (rTRV) was calculated as follows:

228 $$\frac{test - retest}{average\ (test, retest)}$$

229 The individual absolute test-retest variability (aTRV) was calculated as follows:

$$\left|\frac{test - retest}{average\ (test, retest)}\right|$$

In addition, a Bland-Altman analysis was performed to assess the agreement between two measures on an individual level. A Mann-Whitney test was performed to investigate phenotypic differences in SB in autoradiography.

All statistical analyses above were performed with GraphPad Prism (version 9.2.0) statistical software. The Intraclass correlation coefficient (ICC) for the test-retest variability study was calculated with the software JMP Pro 17 (v17.0.0). Group and timepoint interaction was set as fixed effect. Animal ID, timepoint, interaction of animal ID and group, and interaction of animal ID and timepoint, were set as random effects. No effect was identified for either interaction. The ICC was reported as the ratio of the animal variance component for the effect to the sum of positive variance components. One-tailed power analyses were performed in G*Power (v3.1.9.6) with significance level (α) at 0.05, confidence (β) set to 80%. Data are represented as mean ± standard deviation (SD) or as mean ± standard error of the mean (SEM). All tests were two-tailed unless stated otherwise. Statistical significance was set at $p<0.05$ with the following standard abbreviations used to reference p values: ns, not significant; *$p<0.05$; **$p<0.01$; ***$p<0.001$; ****$p<0.0001$.

247 # Results

248 **[^{11}C]CHDI-009R demonstrated high metabolic stability**

249 [^{11}C]CHDI-009R radiometabolite analysis revealed a high stability over time in both brain (e.g.
250 40 min: WT=90.9±8.6%; HET=93.8±2.0%; Fig. 2a) and plasma (e.g. 40 min: WT=95.1±1.7%;
251 HET=96.4±1.2%; Fig. 2b) and with no observable peak other than the intact radioligand (Fig.
252 S1). In addition, the plasma-to-whole-blood ratio was stable over time with no difference
253 observed between genotypes (WT=1.8±0.1; HET=1.7±0.2; Fig. 2c). IDIF profiles of both
254 genotypes displayed a comparable peak within 2 min of radioligand injection and a similar
255 stable signal after 5 min p.i. until the end of acquisition (Fig. 2d). Given the high stability and
256 no difference between genotypes, no corrections were applied to IDIFs for accurate $V_{T\ (IDIF)}$
257 estimations.

258

259 **[^{11}C]CHDI-009R kinetic modeling with 90 min scan duration**

260 The averaged striatal SUV TACs of [^{11}C]CHDI-009R demonstrated rapid penetration into the
261 brain in both genotypes, but a subsequent slower wash-out was observed in the brain in HET
262 animals compared to WTs (Fig. 3a). We further observed an excellent agreement between
263 2TCM quantification and Logan graphical analysis (striatum: r^2=0.996; p<0.0001) with minimal
264 deviation from the identity line (slope = 0.998) (Fig. 3b); thus, supporting the use of Logan
265 graphical analysis to quantify [^{11}C]CHDI-009R in mice.

266 Next, we performed a $V_{T\ (IDIF)}$ time stability analysis to estimate the shortest recommended
267 acquisition time. Although we observed no impact on $V_{T\ (IDIF)}$ in WT animals (Fig. 3c), $V_{T\ (IDIF)}$
268 in HET mice was susceptible to a steady underestimation, which passed the 90% threshold
269 with a 60 min acquisition (Fig. 3d). Thus, shortening the scan acquisition time from 90 min
270 was not recommended to avoid even minimal underestimation of a phenotypic effect. Further,
271 we investigated the impact of injected mass on [^{11}C]CHDI-009R $V_{T\ (IDIF)}$. As shown in Fig. S2,

272 a definite negative association was observed; thus, the recommended upper limit for injectable
273 mass was set to 1.7 μg/kg.
274
275 **[^{11}C]CHDI-009R quantification revealed phenotypic differences**
276 The averaged parametric $V_{T\ (IDIF)}$ maps of WT and HET mice shown in Fig. 4a visualized a
277 clear genotype effect. The two-way ANOVA test revealed a significant genotype effect ($F_{(1, 183)}$
278 = 987.3; p<0.0001) and the Bonferroni *post hoc* analysis demonstrated statistically significant
279 increased signal in HET mice compared to their WT littermates in all tested brain regions
280 (p<0.0001) (Fig. 4b). Phenotypic $V_{T\ (IDIF)}$ differences ranged from 55.5±5.4% in the cerebellum
281 to 105.8±6.2% in the thalamus (Table 1).
282
283 **[^{11}C]CHDI-009R displayed excellent test-retest reproducibility**
284 To measure the reliability of [^{11}C]CHDI-009R, a test-retest study was performed in WT and
285 HET zQ175DN mice at 9 months. Parametric $V_{T\ (IDIF)}$ maps did not reveal any apparent
286 differences between scans (Fig. 5a). The aTRV was overall low, indicating a high reliability,
287 with a range from 5.1±4.0% to 7.7±4.2% in striatum of WT and HET animals (Fig. 5b; Table
288 2). The Bland-Altman plot displayed close-ranged levels of agreement (-16.0% to 14.7%) (Fig.
289 5c). In addition, the regional rTRV, with values ranging from -3.1±8.5% to 4.3±8.3% in WT and
290 from -4.8±6.2% to 1.2±8.3% in HET, demonstrated limited difference across brain regions
291 (Table 2). Overall, according to the ICC values, [^{11}C]CHDI-009R displayed a good to excellent
292 test-retest agreement (Table 2).
293
294 **[^{11}C]CHDI-009R differentiated genotypes at 3 months**
295 In addition to the comprehensive assessment of [^{11}C]CHDI-009R properties at 9 months, a
296 study was performed at 3 months, when less mHTT aggregates are present in HET zQ175DN
297 mice, providing insights into the degree of sensitivity for this radioligand. Based on parametric

298 $V_{T\ (IDIF)}$ maps, an increased signal in HET mice could be detected (Fig. 6a). Accordingly, the
299 two-way ANOVA test revealed a significant genotype effect ($F_{(1, 175)} = 62.3$; $p<0.0001$). The
300 Bonferroni *post hoc* analysis displayed statistically significant phenotypic differences between
301 genotypes, ranging from 8.3±2.7% to 16.3±2.9% in test regions, with the exception of motor
302 cortex (5.0±2.8%; not significant) (Fig. 6b; Table 3). The mHTT aggregate binding capacity of
303 CHDI-009R was also demonstrated through a post-mortem autoradiography study with the
304 tritiated version of the ligand. [^{3}H]CHDI-009R displayed a significantly different SB in HET
305 mice compared to WT littermates (Fig. 6c, $p<0.0001$).
306
307 **[^{11}C]CHDI-009R is suitable for evaluating therapeutic efficacy in zQ175DN mice**
308 We performed power analyses to estimate group sizes needed for evaluating therapeutic
309 efficacy (α=0.05, β=80%) in zQ175DN mice. As shown in Table S4, statistical power was
310 good, as revealed by the range of Cohen's *d* of 0.59 – 1.70 and 3.52 – 5.15 at 3 and 9 months,
311 respectively. This indicated that at 9 months, [^{11}C]CHDI-009R could significantly display a 20%
312 difference in mHTT aggregates with acceptable group arms (e.g. striatum: n=21). At 3 months,
313 however, only in striatum (n=23) and thalamus (n=26) could a larger effect (50% difference)
314 between groups be detected with a similar sample size.
315

316 ## Discussion

317 Here we report the *in vivo* characterization of a novel mHTT aggregate PET radioligand,
318 [^{11}C]CHDI-009R, with higher selectivity [20] than previously investigated radiotracers [12, 15,
319 16]. As in previous evaluation studies of mHTT aggregate radiotracers, we included only male
320 mice for better comparison, as no sex differences have been observed in HET mice before
321 [32]. Since the current study focused on evaluating the capability of [^{11}C]CHDI-009R in
322 detecting different levels of mHTT aggregates in the brain *in vivo*, only one sex was used.
323 While research on sex differences is of significant importance, the inclusion of both sexes in
324 this study was considered secondary.

325 We show that [^{11}C]CHDI-009R rapidly enters the brain, followed by wash-out, indicating its
326 reversible binding. The slower rate of radioligand wash-out from the brain of the HET animals
327 was likely due to the presence of mHTT aggregates that are absent in WT. [^{11}C]CHDI-009R
328 demonstrated high stability in mouse plasma, and no metabolite correction was deemed
329 necessary for IDIFs, although we could only obtain data until 40 min p.i. due to the loss of
330 radioactive signal at later time points in the limited blood sample that can be collected as a
331 consequence of the radioisotope's half-life.

332 The cerebral retention time for both genotypes was suitable for estimating the $V_{T\ (IDIF)}$, for which
333 both 2TCM and Logan graphical analysis were shown as adequate models. The time stability
334 kinetic analysis revealed that a reduction in scan acquisition time was not feasible without
335 introducing a genotype-specific underestimation of the $V_{T\ (IDIF)}$ values, which would result in an
336 artificial decrease of phenotypic differences. The current scan duration of 90 min, however,
337 borders the capability of obtaining data with limited noise due to the short half-life of the isotope
338 (20.4 min), which requires a prompt scan acquisition and keeping the injected mass within the
339 recommended limit of 1.7 μg/kg.

340 With those optimized PET imaging conditions, quantification with Logan indicated that
341 [^{11}C]CHDI-009R could significantly distinguish genotypes at both 9 and 3 months of age, with

342 comparable magnitude as observed with previous mHTT radiotracers [10, 17]. Noteworthy,
343 there was no change in $V_{T\ (IDIF)}$ values of WT animals across brain regions, indicating that
344 [^{11}C]CHDI-009R can reliably and uniformly show the lack of a target in WT animals. Moreover,
345 the post-mortem [^{3}H]CHDI-009R autoradiography confirmed the lack of mHTT aggregates in
346 WT mice, corroborating the previously described findings [20]. This represents an important
347 indication of minimum off-target binding that could otherwise potentially diminish the utility of
348 a radioligand, as shown for several Alzheimer's disease-related radioligands [33].
349 Besides general affinity and selectivity, intra-subject variability was also an important factor to
350 be considered. The reliability of [^{11}C]CHDI-009R was demonstrated by the excellent test-retest
351 performance as determined via Bland-Altman plot and ICC values [34]. This provides a
352 significant benefit for a more accurate application, especially in longitudinal settings, and
353 represents a favorable attribute compared to the poor reliability of [^{18}F]CHDI-650 (ICC: 0.00 –
354 0.27) [17].
355 The capability of detecting early changes at the molecular level represents another important
356 utility in the context of monitoring (early) therapeutic intervention, as described in the studies
357 of HD mouse models [10, 32]. Our current work confirmed the *ex vivo* findings that [^{3}H]-
358 radiolabeled CHDI-009R [20] can detect statistically significant phenotypic differences at 3
359 months of age with both *in vivo* PET imaging and post-mortem autoradiography.
360 We have described several mHTT radiotracers that could identify a significant difference in
361 striatal binding in 3-month-old zQ175DN HET mice [11, 17]. Especially [^{11}C]CHDI-180R
362 exhibited high metabolic stability and appropriate brain wash-out for imaging studies in both
363 HD mouse models as well as in a large non-human primate (NHP) model of HD [35],
364 suggesting [^{11}C]CHDI-180R as a well-performing mHTT aggregate-directed PET radioligand
365 for animal models [10, 14]. However, [^{11}C]CHDI-180R demonstrated high intersubject
366 variability and relatively low signal-to-background ratio in the first-in-patient PET study [19].
367 The increased SB and binding potential of [^{3}H]CHDI-009R (SB=205.3±10.3 fmol/mg; B_{max}=448

368 fmol/mg) compared to [^{3}H]CHDI-180 (SB=70.9±11.0 fmol/mg; B_{max}=163 fmol/mg) in HOM
369 zQ175DN brains likely points towards higher sensitivity to detect mHTT aggregates with
370 CHDI-009R, as shown in post-mortem HD brains [20]. Further, radio-binding assays revealed
371 increased binding to mHTT aggregates with CHDI-009R (IC_{50}=0.4±0.2 nM) in contrast to
372 CHDI-180R (IC_{50}=1.3±1.0 nM), while additionally minimizing the affinity for abeta- and/or tau-
373 associated aggregates [20]. Thus, [^{11}C]CHDI-009R demonstrates high potential for successful
374 clinical translation given its improved characteristics over CHDI-180R. The utility of CHDI-
375 009R as an imaging biomarker will be assessed in a clinical setting.
376

377 ## Conclusions

378 [^{11}C]CHDI-009R is a highly stable radioligand capable of detecting significant phenotypic
379 differences between HET and WT zQ175DN mice at different ages in a reproducible manner.
380 These findings suggest [^{11}C]CHDI-009R to be a suitable radioligand to image mHTT
381 aggregates in mice. Notably, a clinical investigation is underway to determine its suitability for
382 assessing mHTT aggregates in humans.
383

Declarations

Ethics approval

Experiments followed the European Committee (decree 2010/63/CEE) and were approved by the Ethical Committee for Animal Testing (ECD 2019–39) at the University of Antwerp (Belgium).

Availability of data and material

The PET datasets generated or analysed during the current study are available in the OpenNeuro repository, https://doi.org/10.18112/openneuro.ds006613.v1.0.1

Acknowledgements

The authors thank Philippe Joye, Caroline Berghmans, Romy Raeymakers and Eleni Van der Hallen of the Molecular Imaging Center Antwerp (MICA) for their valuable assistance. FZ, LE, AVE, JA, AM, JV, SS, and DB are members of the *μ*Neuro Research Centre of Excellence at the University of Antwerp. The authors acknowledge the contribution of the following CHDI staff: Drs Mette Skinbjerg, Robert Doot and Yuchuan Wang for helpful discussions; Drs Simon Noble and Vahri Beaumont for reviewing and providing constructive feedback; Brenda Lager for coordinating animal supply and Braden Boone for project management.

Authors' contributions

Conceptualization: JV, VK, JB, LL, SS, DB

Methodology: JV, AM, SS, DB

Data acquisition: FZ, LE, AVE, SDL

Formal analysis and investigation: FZ, LE, AVE

Data interpretation: FZ, JV, JA, VK, JB, LL, SS, DB

Writing – original draft preparation: FZ, SS, DB

410 Writing – review and editing: FZ, JV, SDL, JA, CD, VK, JB, LL, SS, DB

411 Resources: CD, VK, JB, LL, SS, DB

412 Funding acquisition: SS, DB

413 Supervision: JV, SS, DB

414

415 **Competing interests**

416 This work was funded by CHDI Foundation, Inc., a privately-funded nonprofit biomedical
417 research organization exclusively dedicated to collaboratively developing therapeutics that
418 improve the lives of those affected by Huntington's disease. CD, VK, JB, and LL are employed
419 by CHDI Management, Inc., the company that manages the scientific activities of CHDI
420 Foundation. No other potential conflicts of interest relevant to this article exist.

421

422 **Funding**

423 This work was funded by CHDI Foundation, Inc. under agreement number A-11627. DB
424 acknowledges support by the Research Foundation Flanders (FWO) (ID: 1229721N).
425 University of Antwerp supported the work through professorships for JV, SS, and DB.

426

References

1. Saudou, F. and Humbert, S., *The Biology of Huntingtin.* Neuron, 2016. **89**(5): p. 910-26.
2. The-Huntington's-Disease-Collaborative-Research-Group, *A novel gene containing a trinucleotide repeat that is expanded and unstable on Huntington's disease chromosomes.* Cell, 1993. **72**(6): p. 971-983.
3. McColgan, P. and Tabrizi, S.J., *Huntington's disease: a clinical review.* Eur J Neurol, 2018. **25**(1): p. 24-34.
4. Waldvogel, H.J., Kim, E.H., Tippett, L.J., Vonsattel, J.P., and Faull, R.L., *The Neuropathology of Huntington's Disease.* Curr Top Behav Neurosci, 2015. **22**: p. 33-80.
5. Tabrizi, S.J., Ghosh, R., and Leavitt, B.R., *Huntingtin Lowering Strategies for Disease Modification in Huntington's Disease.* Neuron, 2019. **101**(5): p. 801-819.
6. Wild, E.J. and Tabrizi, S.J., *Therapies targeting DNA and RNA in Huntington's disease.* The Lancet Neurology, 2017. **16**(10): p. 837-847.
7. Saade, J. and Mestre, T.A., *Huntington's Disease: Latest Frontiers in Therapeutics.* Curr Neurol Neurosci Rep, 2024. **24**(8): p. 255-264.
8. Caron, N.S., Banos, R., Aly, A.E., Xie, Y., Ko, S., Potluri, N., Anderson, C., Black, H.F., Anderson, L.M., Gordon, B., Southwell, A.L., and Hayden, M.R., *Cerebrospinal fluid mutant huntingtin is a biomarker for huntingtin lowering in the striatum of Huntington disease mice.* Neurobiol Dis, 2022. **166**: p. 105652.
9. Kordasiewicz, H.B., Stanek, L.M., Wancewicz, E.V., Mazur, C., McAlonis, M.M., Pytel, K.A., Artates, J.W., Weiss, A., Cheng, S.H., Shihabuddin, L.S., Hung, G., Bennett, C.F., and Cleveland, D.W., *Sustained therapeutic reversal of Huntington's disease by transient repression of huntingtin synthesis.* Neuron, 2012. **74**(6): p. 1031-44.
10. Bertoglio, D., Bard, J., Hessmann, M., Liu, L., Gartner, A., De Lombaerde, S., Huscher, B., Zajicek, F., Miranda, A., Peters, F., Herrmann, F., Schaertl, S., Vasilkovska, T., Brown, C.J., Johnson, P.D., Prime, M.E., Mills, M.R., Van der Linden, A., Mrzljak, L., Khetarpal, V., Wang, Y., Marchionini, D.M., Skinbjerg, M., Verhaeghe, J., Dominguez, C., Staelens, S., and Munoz-Sanjuan, I., *Development of a ligand for in vivo imaging of mutant huntingtin in Huntington's disease.* Sci Transl Med, 2022. **14**(630): p. eabm3682.
11. Bertoglio, D., Verhaeghe, J., Miranda, A., Wyffels, L., Stroobants, S., Mrzljak, L., Khetarpal, V., Skinbjerg, M., Liu, L., Dominguez, C., Munoz-Sanjuan, I., Bard, J., and Staelens, S., *Longitudinal preclinical evaluation of the novel radioligand [11C]CHDI-626 for PET imaging of mutant huntingtin aggregates in Huntington's disease.* Eur J Nucl Med Mol Imaging, 2022. **49**(4): p. 1166-1175.
12. Herrmann, F., Hessmann, M., Schaertl, S., Berg-Rosseburg, K., Brown, C.J., Bursow, G., Chiki, A., Ebneth, A., Gehrmann, M., Hoeschen, N., Hotze, M., Jahn, S., Johnson, P.D., Khetarpal, V., Kiselyov, A., Kottig, K., Ladewig, S., Lashuel, H., Letschert, S., Mills, M.R., Petersen, K., Prime, M.E., Scheich, C., Schmiedel, G., Wityak, J., Liu, L., Dominguez, C., Munoz-Sanjuan, I., and Bard, J.A., *Pharmacological characterization of mutant huntingtin aggregate-directed PET imaging tracer candidates.* Sci Rep, 2021. **11**(1): p. 17977.

13. Liu, L., Johnson, P.D., Prime, M.E., Khetarpal, V., Lee, M.R., Brown, C.J., Chen, X., Clark-Frew, D., Coe, S., Conlon, M., Davis, R., Ensor, S., Esposito, S., Moren, A.F., Gai, X., Green, S., Greenaway, C., Haber, J., Halldin, C., Hayes, S., Herbst, T., Herrmann, F., Hessmann, M., Hsai, M.M., Kotey, A., Mangette, J.E., Mills, M.R., Monteagudo, E., Nag, S., Nibbio, M., Orsatti, L., Schaertl, S., Scheich, C., Sproston, J., Stepanov, V., Varnas, K., Varrone, A., Wityak, J., Mrzljak, L., Munoz-Sanjuan, I., Bard, J.A., and Dominguez, C., *[(11)C]CHDI-626, a PET Tracer Candidate for Imaging Mutant Huntingtin Aggregates with Reduced Binding to AD Pathological Proteins.* J Med Chem, 2021. **64**(16): p. 12003-12021.
14. Bertoglio, D., Weiss, A.R., Liguore, W., Martin, L.D., Hobbs, T., Templon, J., Srinivasan, S., Dominguez, C., Munoz-Sanjuan, I., Khetarpal, V., Verhaeghe, J., Staelens, S., Link, J., Liu, L., Bard, J.A., and McBride, J.L., *In Vivo Cerebral Imaging of Mutant Huntingtin Aggregates Using (11)C-CHDI-180R PET in a Nonhuman Primate Model of Huntington Disease.* J Nucl Med, 2023. **64**(10): p. 1581-1587.
15. Liu, L., Prime, M.E., Lee, M.R., Khetarpal, V., Brown, C.J., Johnson, P.D., Miranda-Azpiazu, P., Chen, X., Clark-Frew, D., Coe, S., Davis, R., Dickie, A., Ebneth, A., Esposito, S., Gadouleau, E., Gai, X., Galan, S., Green, S., Greenaway, C., Giles, P., Halldin, C., Hayes, S., Herbst, T., Herrmann, F., Hessmann, M., Jia, Z., Kiselyov, A., Kotey, A., Krulle, T., Mangette, J.E., Marston, R.W., Menta, S., Mills, M.R., Monteagudo, E., Nag, S., Nibbio, M., Orsatti, L., Schaertl, S., Scheich, C., Sproston, J., Stepanov, V., Svedberg, M., Takano, A., Taylor, M., Thomas, W., Toth, M., Vaidya, D., Vanras, K., Weddell, D., Wigginton, I., Wityak, J., Mrzljak, L., Munoz-Sanjuan, I., Bard, J.A., and Dominguez, C., *Imaging Mutant Huntingtin Aggregates: Development of a Potential PET Ligand.* J Med Chem, 2020. **63**(15): p. 8608-8633.
16. Liu, L., Johnson, P.D., Prime, M.E., Khetarpal, V., Brown, C.J., Anzillotti, L., Bertoglio, D., Chen, X., Coe, S., Davis, R., Dickie, A.P., Esposito, S., Gadouleau, E., Giles, P.R., Greenaway, C., Haber, J., Halldin, C., Haller, S., Hayes, S., Herbst, T., Herrmann, F., Hessmann, M., Hsai, M.M., Khani, Y., Kotey, A., Lembo, A., Mangette, J.E., Marriner, G.A., Marston, R.W., Mills, M.R., Monteagudo, E., Forsberg-Moren, A., Nag, S., Orsatti, L., Sandiego, C., Schaertl, S., Sproston, J., Staelens, S., Tookey, J., Turner, P.A., Vecchi, A., Veneziano, M., Munoz-Sanjuan, I., Bard, J., and Dominguez, C., *Design and Evaluation of [(18)F]CHDI-650 as a Positron Emission Tomography Ligand to Image Mutant Huntingtin Aggregates.* J Med Chem, 2023. **66**(1): p. 641-656.
17. Zajicek, F., Verhaeghe, J., De Lombaerde, S., Van Eetveldt, A., Miranda, A., Munoz-Sanjuan, I., Dominguez, C., Khetarpal, V., Bard, J., Liu, L., Staelens, S., and Bertoglio, D., *Preclinical evaluation of the novel [(18)F]CHDI-650 PET ligand for non-invasive quantification of mutant huntingtin aggregates in Huntington's disease.* Eur J Nucl Med Mol Imaging, 2024. **52**(1): p. 122-133.
18. Delva, A., Koole, M., Serdons, K., Bormans, G., Liu, L., Bard, J., Khetarpal, V., Dominguez, C., Munoz-Sanjuan, I., Wood, A., Skinbjerg, M., Wang, Y., Vandenberghe, W., and Van Laere, K., *Biodistribution and dosimetry in human healthy volunteers of the PET radioligands [(11)C]CHDI-00485180-R and [(11)C]CHDI-00485626, designed for quantification of cerebral aggregated mutant huntingtin.* Eur J Nucl Med Mol Imaging, 2022. **50**(1): p. 48-60.

19. Delva, A., Koole, M., Serdons, K., Bormans, G., Skinbjerg, M., Khetarpal, V., Liu, L., Bard, J., Doot, R., Warner, J.H., Sathe, S., Sampaio, C., Wood, A., Van Laere, K., and Vandenberghe, W., *PET imaging with [(1)(1)C]CHDI-00485180-R, designed as radioligand for aggregated mutant huntingtin, in people with Huntington's disease.* Eur J Nucl Med Mol Imaging, 2025.
20. Liu, L., Johnson, P.D., Mills, M.R., Turner, P.A., Prime, M.E., Brown, C.J., Kotey, A., Coe, S., Giles, P.R., Lloyd, C., Hayes, S., Marlin, F.J., Rota, F., Herrmann, F., Hessmann, M., Schaertl, S., Zajicek, F., De Lombaerde, S., Elvas, F., Verhaeghe, J., Staelens, S., Bertoglio, D., Chen, X., Conlon, M.P., Davis, R., Ensor, S.F., Haber, J., Haber, K.C., Hsai, M.M., Mangette, J.E., Penniman, W.F., Anzillotti, L., Esposito, S., Lembo, A., Orsatti, L., Ventre, D., Veneziano, M., Sandiego, C., Haller, S., Marriner, G.A., Munoz-Sanjuan, I., Khetarpal, V., Bard, J.A., and Dominguez, C., *Isoindolinone-Based PET Tracers for Imaging Mutant Huntingtin Aggregates.* J Med Chem, 2025. **68**(14): p. 14818-14842.
21. Menalled, L.B., Kudwa, A.E., Miller, S., Fitzpatrick, J., Watson-Johnson, J., Keating, N., Ruiz, M., Mushlin, R., Alosio, W., McConnell, K., Connor, D., Murphy, C., Oakeshott, S., Kwan, M., Beltran, J., Ghavami, A., Brunner, D., Park, L.C., Ramboz, S., and Howland, D., *Comprehensive behavioral and molecular characterization of a new knock-in mouse model of Huntington's disease: zQ175.* PLoS One, 2012. **7**(12): p. e49838.
22. Heikkinen, T., Lehtimaki, K., Vartiainen, N., Puolivali, J., Hendricks, S.J., Glaser, J.R., Bradaia, A., Wadel, K., Touller, C., Kontkanen, O., Yrjanheikki, J.M., Buisson, B., Howland, D., Beaumont, V., Munoz-Sanjuan, I., and Park, L.C., *Characterization of neurophysiological and behavioral changes, MRI brain volumetry and 1H MRS in zQ175 knock-in mouse model of Huntington's disease.* PLoS One, 2012. **7**(12): p. e50717.
23. Cudalbu, C., McLin, V.A., Lei, H., Duarte, J.M., Rougemont, A.L., Oldani, G., Terraz, S., Toso, C., and Gruetter, R., *The C57BL/6J mouse exhibits sporadic congenital portosystemic shunts.* PLoS One, 2013. **8**(7): p. e69782.
24. Bertoglio, D., Verhaeghe, J., Miranda, A., Kertesz, I., Cybulska, K., Korat, S., Wyffels, L., Stroobants, S., Mrzljak, L., Dominguez, C., Liu, L., Skinbjerg, M., Munoz-Sanjuan, I., and Staelens, S., *Validation and noninvasive kinetic modeling of [(11)C]UCB-J PET imaging in mice.* J Cereb Blood Flow Metab, 2020. **40**(6): p. 1351-1362.
25. Miranda, A., Bertoglio, D., Glorie, D., Stroobants, S., Staelens, S., and Verhaeghe, J., *Validation of a spatially variant resolution model for small animal brain PET studies.* Biomed Phys Eng Express, 2020. **6**(4): p. 045001.
26. Bertoglio, D., Verhaeghe, J., Kosten, L., Thomae, D., Van der Linden, A., Stroobants, S., Wityak, J., Dominguez, C., Mrzljak, L., and Staelens, S., *MR-based spatial normalization improves [18F]MNI-659 PET regional quantification and detectability of disease effect in the Q175 mouse model of Huntington's disease.* PLoS One, 2018. **13**(10): p. e0206613.
27. Johnson, G.A., Badea, A., Brandenburg, J., Cofer, G., Fubara, B., Liu, S., and Nissanov, J., *Waxholm space: an image-based reference for coordinating mouse brain research.* Neuroimage, 2010. **53**(2): p. 365-72.
28. Bertoglio, D., Verhaeghe, J., Korat, S., Miranda, A., Wyffels, L., Stroobants, S., Mrzljak, L., Dominguez, C., Liu, L., Skinbjerg, M., Munoz-Sanjuan, I., and

Staelens, S., *In vitro and In vivo Assessment of Suitable Reference Region and Kinetic Modelling for the mGluR1 Radioligand [(11)C]ITDM in Mice.* Mol Imaging Biol, 2020. **22**(4): p. 854-863.

29. Bertoglio, D., Zajicek, F., Lombaerde, S., Miranda, A., Stroobants, S., Wang, Y., Dominguez, C., Munoz-Sanjuan, I., Bard, J., Liu, L., Verhaeghe, J., and Staelens, S., *Validation, kinetic modeling, and test-retest reproducibility of [(18)F]SynVesT-1 for PET imaging of synaptic vesicle glycoprotein 2A in mice.* J Cereb Blood Flow Metab, 2022. **42**(10): p. 1867-1878.
30. Verhaeghe, J., Bertoglio, D., Kosten, L., Thomae, D., Verhoye, M., Van Der Linden, A., Wyffels, L., Stroobants, S., Wityak, J., Dominguez, C., Mrzljak, L., and Staelens, S., *Noninvasive Relative Quantification of [(11)C]ABP688 PET Imaging in Mice Versus an Input Function Measured Over an Arteriovenous Shunt.* Front Neurol, 2018. **9**: p. 516.
31. Paxinos, G. and Franklin, K.B.J., *The mouse brain in stereotaxic coordinates: Academic Press*. 2 edition ed. 2003.
32. Marchionini, D.M., De Lombaerde, S., van Rijswijk, J., Zajicek, F., Everix, L., Miranda, A., Aaltonen, M.J., Kluger, C.M., Wild, T., Kakoulidou, A., Gundelach, J., Fieblinger, T., Fentz, J., Rosinski, J., Obenauer, J., Greene, J.R., Liu, L., Munoz-Sanjuan, I., Verhoye, M., Verhaeghe, J., Bard, J., Staelens, S., and Bertoglio, D., *Pharmacodynamic biomarkers responsive to mutant huntingtin lowering in a Huntington's disease mouse model.* Neurobiol Dis, 2025. **209**: p. 106906.
33. Cassinelli Petersen, G., Roytman, M., Chiang, G.C., Li, Y., Gordon, M.L., and Franceschi, A.M., *Overview of tau PET molecular imaging.* Curr Opin Neurol, 2022. **35**(2): p. 230-239.
34. Cicchetti, D., *Guidelines, Criteria, and Rules of Thumb for Evaluating Normed and Standardized Assessment Instruments in Psychology.* Psychological Assessment, 1994. **6**(4): p. 284-290.
35. Weiss, A.R., Liguore, W.A., Brandon, K., Wang, X., Liu, Z., Domire, J.S., Button, D., Srinivasan, S., Kroenke, C.D., and McBride, J.L., *A novel rhesus macaque model of Huntington's disease recapitulates key neuropathological changes along with motor and cognitive decline.* Elife, 2022. **11**.

603 # Tables

604 ***Table 1 [^{11}C]CHDI-009R $V_{T\ (IDIF)}$ (Logan) [mL/cm^3] quantitative values in 9-month-old mice***

605

	WT (mean±SD)	HET (mean±SD)	*Post hoc* *p* value	Δ±SE [%]
Striatum	0.46±0.05	0.90±0.11	<0.0001	94.6±6.2
Motor Cortex	0.47±0.06	0.88±0.13	<0.0001	88.8±6.3
Hippocampus	0.45±0.04	0.83±0.11	<0.0001	85.9±6.4
Thalamus	0.46±0.05	0.94±0.13	<0.0001	105.8±6.2
Cerebellum	0.52±0.06	0.81±0.10	<0.0001	55.5±5.4

606

607

608

609

610 WT: *n*=20; HET: *n*=19. SD = standard deviation; Δ = phenotypic difference; SE = standard error

611

612 ***Table 2 [^{11}C]CHDI-009R test-retest $V_{T\,(IDIF)}$ values and relative and absolute test-retest***

613 ***variability in 9-month-old mice***

	Test $V_{T\,(IDIF)}$ (Logan) [mL/cm^3]		Retest $V_{T\,(IDIF)}$ (Logan) [mL/cm^3]		rTRV [%]		aTRV [%]		ICC
	WT	**HET**	**WT**	**HET**	**WT**	**HET**	**WT**	**HET**	
Striatum	0.45±0.04	0.84±0.06	0.46±0.04	0.82±0.10	-0.9±6.7	0.9±9.2	5.1±4.0	7.7±4.2	0.62
Motor Cortex	0.49±0.04	0.79±0.07	0.47±0.03	0.84±0.12	4.3±8.3	-4.8±6.2	7.0±5.8	6.3± 4.5	0.79
Hippocampus	0.43±0.04	0.77±0.06	0.44±0.04	0.66±0.04	-1.8± 7.4	1.2 ± 8.3	6.1± 4.2	6.9± 4.1	0.71
Thalamus	0.44±0.03	0.84±0.07	0.46±0.04	0.81±0.08	-3.1±8.5	-0.1±7.8	6.2± 6.2	5.2±5.4	0.72
Cerebellum	0.49±0.04	0.72±0.05	0.50±0.05	0.67±0.04	-2.1± 8.3	-0.1± 8.0	6.2± 5.5	6.3± 4.2	0.63

614

615 *rTRV = relative test-retest variability; aTRV = absolute test-retest variability; ICC = Intraclass*

616 *correlation coefficient. Data is given as mean±SD. WT: n=8; HET: n=8*

617

618 ***Table 3 [^{11}C]CHDI-009R $V_{T\ (IDIF)}$* (Logan) [mL/cm^3] *quantitative values in 3-month-old mice***

619
620
621
622
623
624

	WT (mean±SD)	HET (mean±SD)	*Post hoc* *p* value	Δ±SE [%]
Striatum	0.46±0.03	0.52±0.04	0.0002	12.3±2.9
Motor Cortex	0.47±0.04	0.50±0.06	0.3989	5.0±2.8
Hippocampus	0.44±0.03	0.48±0.04	0.0194	8.9±3.0
Thalamus	0.46±0.03	0.53±0.05	<0.0001	16.3±2.9
Cerebellum	0.50±0.03	0.54±0.04	0.0104	8.3±2.7

625 *WT: n=18; HET: n=19. SD = standard deviation; Δ = phenotypic difference; SE = standard error*

626

627 **Figures**

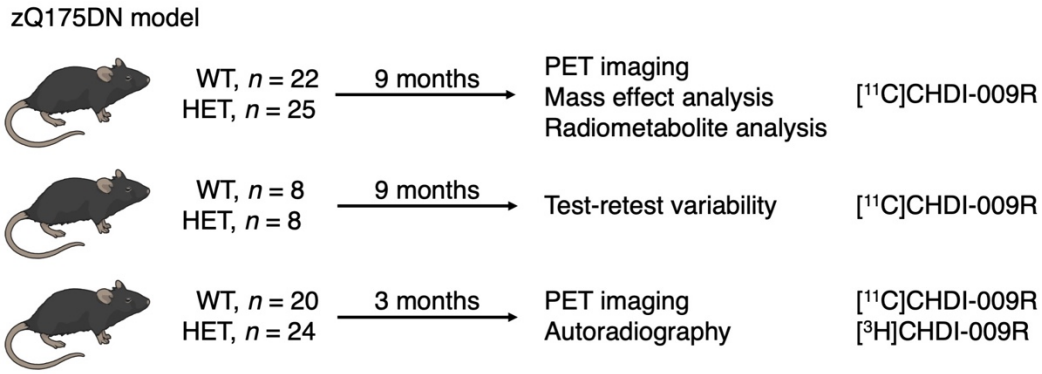

628

629 ***Fig. 1*** *Overview of the experimental design. Number and age of each experimental group for the*

630 *different experimental setups. HET = heterozygous; n = number; WT = wildtype*

631

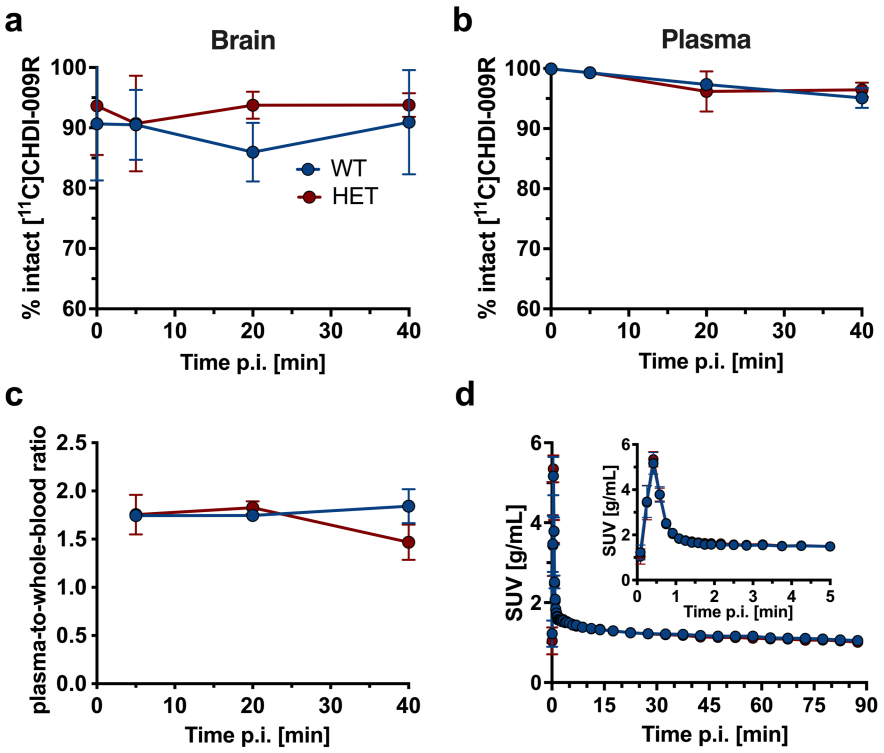

632

633 ***Fig. 2*** *[11C]CHDI-009R brain and plasma analysis and IDIF of WT and HET zQ175DN mice. The*

634 *intact radioligand in percentage for brain (a) and plasma (b) over time. c, Plasma-to-whole-blood*

635 *ratio over time in both genotypes. d, Averaged IDIF SUV curves over 90 min scan time for both*

636 *genotypes. d: Data are represented as mean±SEM. a-c: n=2-5 per genotype and timepoint; d: WT:*

637 *n=20; HET: n=19*

638

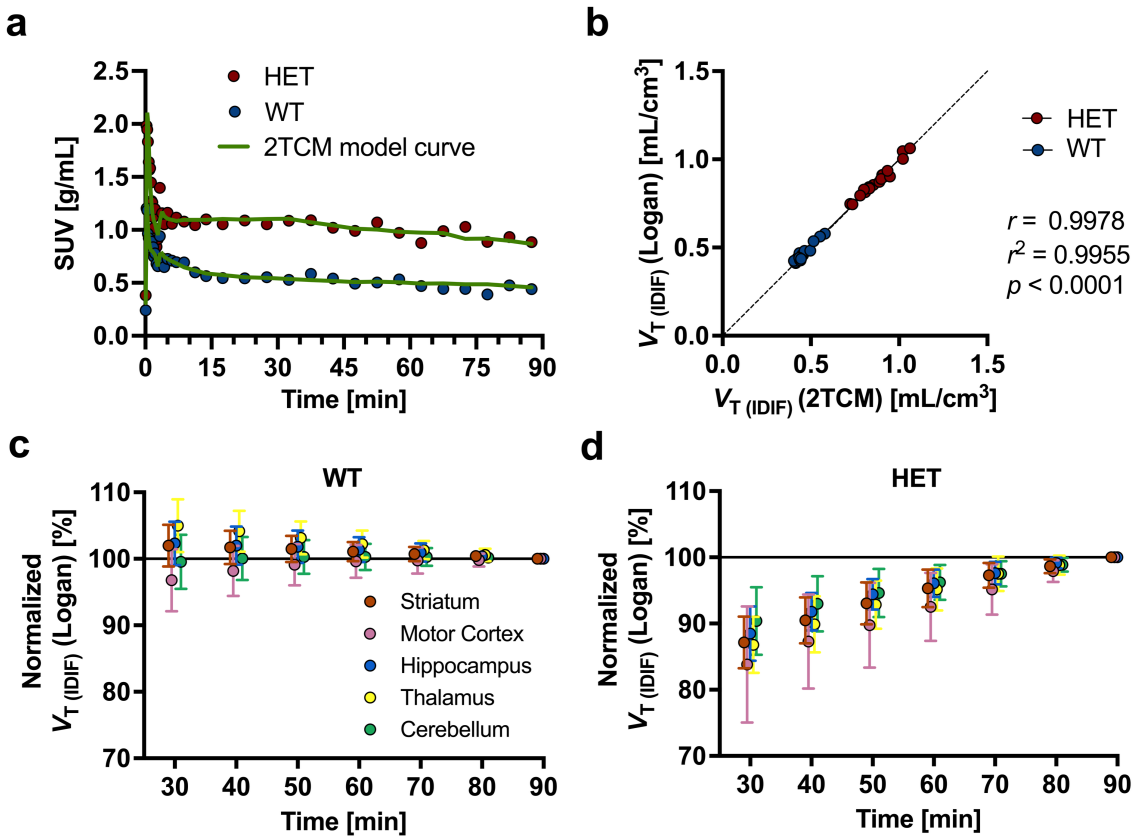

Fig. 3 *[^{11}C]CHDI-009R brain kinetic modeling and $V_{T\ (IDIF)}$ time stability with Logan. a, Exemplary striatal SUV TAC curves of WT and HET animals fitted to 2TCM. b, Pearson's correlation of striatal $V_{T\ (IDIF)}$ values with 2TCM and Logan for verification with simple linear regression. $V_{T\ (IDIF)}$ time stability of Logan in WT (c) and HET (d) mice. $V_{T\ (IDIF)}$ values were normalized to the 90 min scan acquisition time. b-d: WT: n=20; HET: n=19*

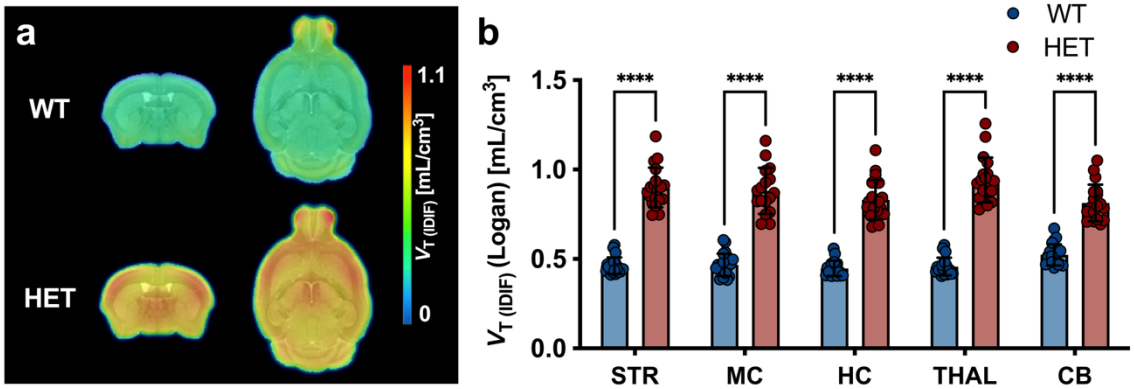

Fig. 4 *[^{11}C]CHDI-009R mHTT aggregate quantification in 9-month-old mice. a, Group-averaged parametric maps for WT and HET zQ175DN mice overlaid onto MRI template. b, [^{11}C]CHDI-009R $V_{T\ (IDIF)}$ estimations in WT and HET mice. Two-way ANOVA with post hoc Bonferroni for multiple comparisons. ****p<0.0001. WT: n=20; HET: n=19. STR = Striatum; MC = Motor Cortex; HC = Hippocampus; THAL = Thalamus; CB = Cerebellum*

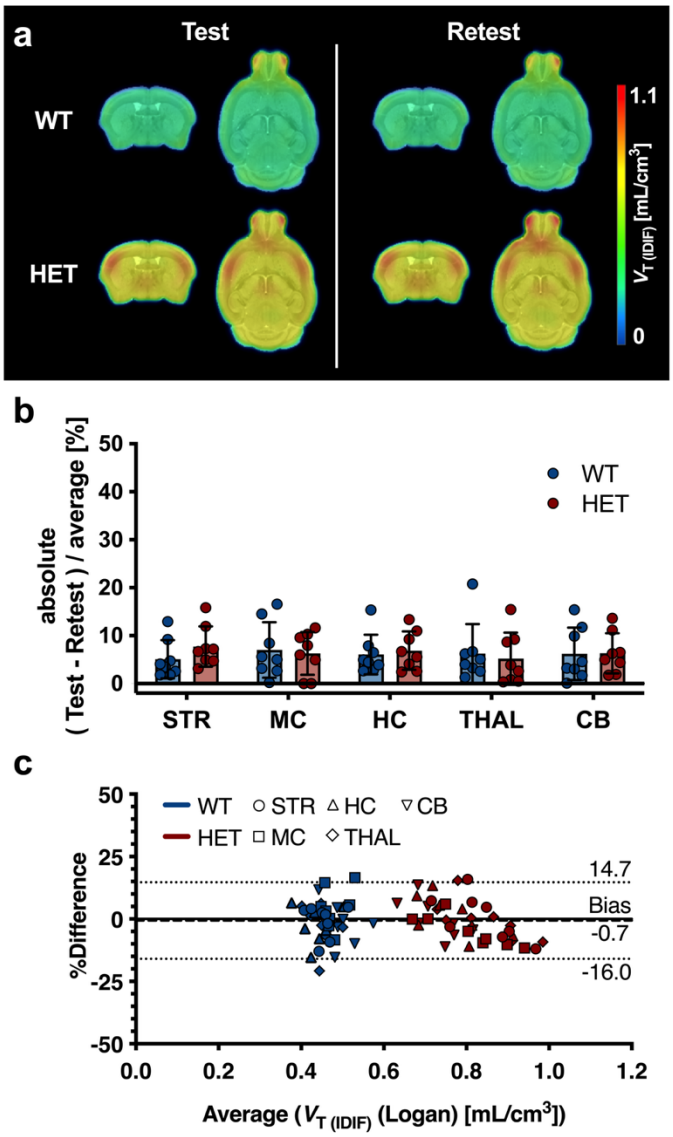

653

654 ***Fig. 5*** *[^{11}C]CHDI-009R test-retest variability analysis in 9-month-old mice. a, Group-averaged*
655 *parametric maps for WT and HET zQ175DN mice at test and retest overlaid onto MRI template.*
656 *b, Absolute test-retest variability analysis in percentage. c, Bland-Altman plot to display the level*
657 *of agreement between test and retest. WT: n=8; HET: n=8. STR = Striatum; MC = Motor Cortex;*
658 *HC = Hippocampus; THAL = Thalamus; CB = Cerebellum*

659

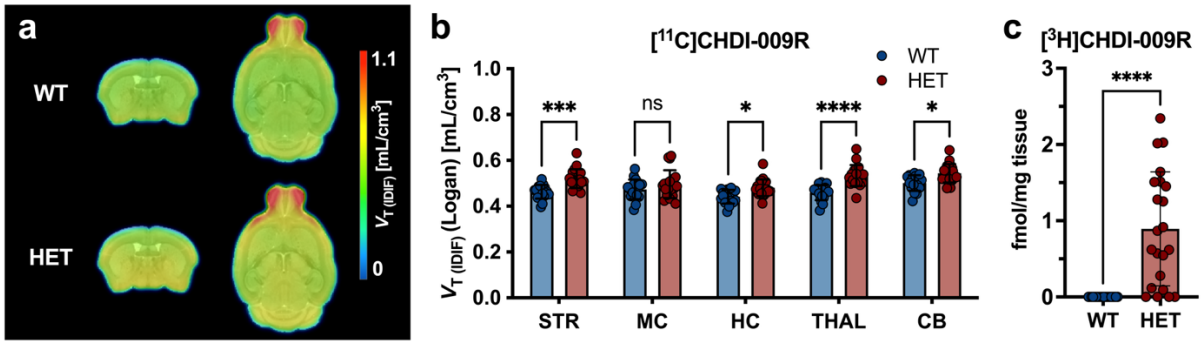

Fig. 6 *mHTT quantification in 3-month-old mice. a, Group-averaged parametric maps for WT and HET zQ175DN mice overlaid onto MRI template. b, [^{11}C]CHDI-009R $V_{T\ (IDIF)}$ estimations in WT and HET mice. c, [^{3}H]CHDI-009R autoradiography of the whole brain in the same mice. ns=not significant; * p<0.05; *** p<0.001; **** p<0.0001. a and b: WT: n=18; HET: n=19; c: WT: n=20; HET: n=22. STR = Striatum; MC = Motor Cortex; HC = Hippocampus; THAL = Thalamus; CB = Cerebellum*

668 **Supplemental material**

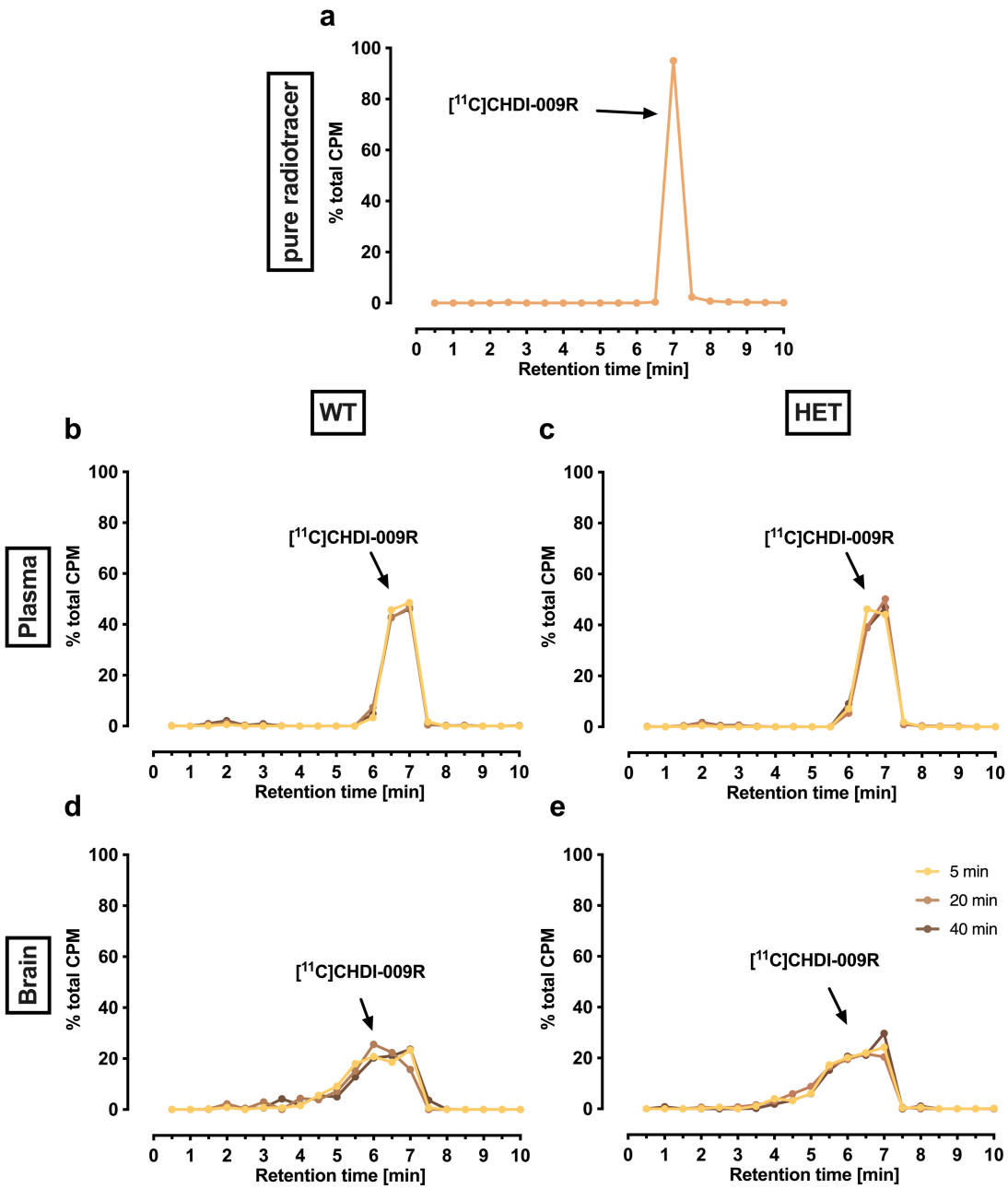

669

670 ***Fig. S1 [11C]CHDI-009R radiometabolite analysis in WT and HET zQ175DN mice.*** *a, Decay-*

671 *corrected reconstructed radiochromatogram for the pure tracer. Decay-corrected reconstructed*

672 *radiochromatograms for all time points in plasma (b and c) and brain (d and e) for WT (b and d)*

673 *and HET mice (c and e). Data is given as the mean. n=2-3 per time point and genotype. CPM =*

674 *counts per minute*

675

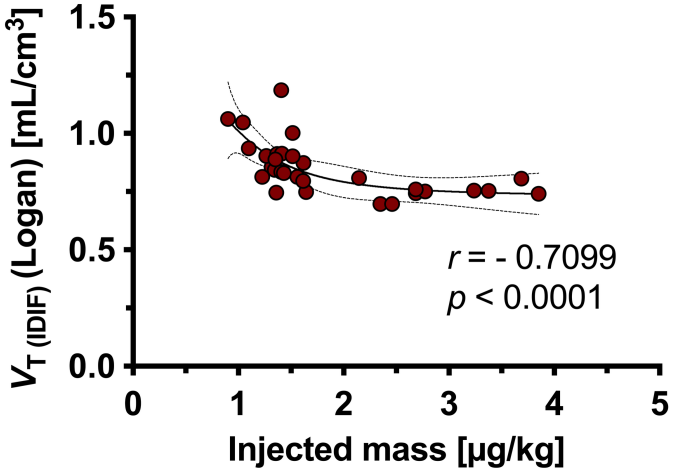

Fig. S2 Mass dose effect in striatum of HET zQ175DN mice at 9 months. *Spearman's correlation of injected masses (µg/kg) and striatal Logan $V_{T\ (IDIF)}$ values. The sigmoidal interpolation (sigmoidal, 4PL, X is concentration) estimates the influence of higher injected masses on the $V_{T\ (IDIF)}$ value. The upper mass dose limit was recommended to be 1.7µg/kg. Data is represented as individual points. n=30*

683 ***Table S1 Scan parameters during the PET imaging study in WT and HET zQ175DN mice***

684 ***for the test-retest study at 9 months***

	Test	Retest		Test	Retest	
	WT (*n* = 8)		***p* value**	**HET (*n* = 8)**		***p* value**
Injected activity (MBq)	6.3±1.6	7.1±2.5	0.1507	5.3±1.7	5.7±2.2	0.5148
A_m (GBq/μmol) at EOS	112.6±28.6	122.8±26.9	0.3682	107.9±30.6	111.2±24.8	0.9375
Weight (g)	34.8±3.4	33.9±2.8	0.0006	30.8±2.6	30.1±2.2	0.0023
Age (d)	257.5±7.5	261.0±10.4	<0.0001	261.1±9.5	267.0±13.9	0.0143
Injected mass (μg/kg)	1.31±0.15	1.27±0.17	0.6242	1.27±0.14	1.22±0.14	0.9275

685

686 Data is given as mean±SD. Unpaired t-test for comparison of genotypes. A_m = molar activity;

687 EOS = end of synthesis

688

689 ***Table S2 Animal and dose parameters for the PET imaging study in WT and HET zQ175DN***

690 ***mice for the evaluation at 9 months***

691

692

693

694

695

696

697

	WT (*n* = 20)	HET (*n* = 19)	*p* value
Injected activity (MBq)	3.8±0.6	4.5 ± 1.2	0.0062
A_m (GBq/μmol) at EOS	71.2±16.1	73.2 ± 16.8	0.7122
Weight (g)	29.7±1.8	34.8 ± 2.8	<0.0001
Age (d)	263.3±4.3	263.2 ± 2.7	0.9221
Injected mass (μg/kg)	1.38 ± 0.20	1.35 ± 0.28	0.9337

698 Data is given as mean±SD unless stated otherwise. Unpaired t-test for comparison of genotypes.

699 A_m = molar activity; EOS = end of synthesis

700

701 ***Table S3 Animal and dose parameters for the PET imaging study in WT and HET zQ175DN***

702 ***mice for the evaluation at 3 months***

703

	WT (*n* = 18)	HET (*n* = 19)	*p* value
Injected activity (MBq)	5.0±0.9	4.8±0.9	0.4608
A_m (GBq/μmol) at EOS	100.8±16.6	99.1±17.9	0.7676
Weight (g)	28.4±2.2	27.7±1.8	0.2975
Age (d)	108.0±3.3	106.6±4.1	0.2523
Injected mass (μg/kg)	1.31 ± 0.14	1.34 ± 0.19	0.6164

704

705

706

707

708

709 Data is given as mean±SD. Unpaired t-test for comparison of genotypes. A_m = molar activity;

710 EOS = end of synthesis

711

712 ***Table S4 [^{11}C]CHDI-009R power analysis of 3- and 9-month-old mice***

age [M]	Brain region	striatal Δ±SE [%]	Cohen's *d*	10%	20%	30%	40%	50%	100%
3	**Striatum**	12.3±2.9	1.70	551	139	62	36	23	6
	Motor Cortex	5.0±2.8	0.59	4947	1238	540	310	199	37
	Hippocampus	8.9±3.0	1.13	1238	310	136	78	51	11
	Thalamus	16.3±2.9	1.70	632	159	70	41	26	6
	Cerebellum	8.3±2.7	1.13	1238	310	136	78	51	11
9	**Striatum**	95.8±6.1	5.15	78	21	10	6	4	2
	Motor Cortex	88.8±6.3	4.05	125	32	15	9	6	2
	Hippocampus	85.9±6.4	4.59	105	27	13	8	5	2
	Thalamus	105.8±6.2	4.87	92	24	11	7	5	2
	Cerebellum	55.5±5.4	3.52	148	38	17	10	7	3

713

714 *One-tailed power analysis with α=0.05 and β=80%. Animal numbers needed for significance*

715 *between treated and non-treated HET groups in a mHTT-lowering study. 100% equals difference*

716 *between non-treated HET and WT groups. 3 months: WT: n=18; HET: n=19; 9 months: WT:*

717 *n=20; HET: n=19. M = months; Δ = phenotypic difference; SE = standard error*

718